Ferroplasmons: Intense Localized Surface Plasmons in Metal-Ferromagnetic Nanoparticles

Ritesh Sachan,[†] Abhinav Malasi,[‡] Jingxuan Ge,[†] Sagar Yadavali,[‡] Hare Krishna,[§] Anup Gangopadhyay,[§] Hernando Garcia,[⊥] Gerd Duscher,[†,∥,*] and Ramki Kalyanaraman[†,‡,*]

[†]Department of Materials Science and Engineering, University of Tennessee, Knoxville, Tennessee 37996, United States, [‡]Department of Chemical and Biomolecular Engineering, University of Tennessee, Knoxville, Tennessee 37996, United States, [§]Department of Physics, Washington University, St. Louis, Missouri 63130, United States, [⊥]Department of Physics, Southern Illinois University, Edwardsville, Illinois 62026, United States, and [∥]Materials Science and Technology Division, Oak Ridge National Laboratory, Oak Ridge, Tennessee 37831, United States

ABSTRACT Interaction of photons with matter at length scales far below their wavelengths has given rise to many novel phenomena, including localized surface plasmon resonance (LSPR). However, LSPR with narrow bandwidth (BW) is observed only in a select few noble metals, and ferromagnets are not among them. Here, we report the discovery of LSPR in ferromagnetic Co and CoFe alloy (8% Fe) in contact with Ag in the form of bimetallic nanoparticles prepared by pulsed laser dewetting. These plasmons in metal-ferromagnetic nanostructures, or ferroplasmons (FP) for short, are in the visible spectrum with comparable intensity and BW to those of the LSPRs from the Ag regions. This finding was enabled by electron energy-loss mapping across individual nanoparticles in a monochromated scanning transmission electron microscope. The appearance of the FP is likely due to plasmonic interaction between the contacting Ag and Co nanoparticles. Since there is no previous evidence for materials that simultaneously show ferromagnetism and such intense LSPRs, this discovery may lead to the design of improved plasmonic materials and applications. It also demonstrates that materials with interesting plasmonic properties can be synthesized using bimetallic nanostructures in contact with each other.

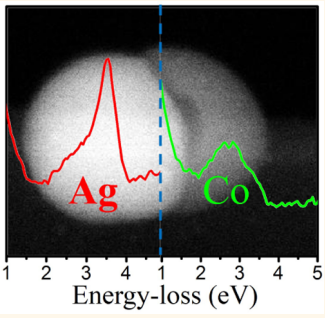

KEYWORDS: localized surface plasmon resonance · electron energy-loss spectroscopy · bimetallic nanoparticles · hybridization · silver · scanning transmission electron microscopy · ferromagnet

Plasmons in metallic systems are coherent collective oscillations of the conduction electrons, which resonate at characteristic frequencies of the material, known as the plasmon frequency. Materials and structures with such responses are used in numerous applications, including in detecting trace amounts of chemicals such as anthrax bacteria[1] and trinitrotoluene (TNT),[2] in surface enhanced Raman scattering detection of DNA and other biological molecules,[3,4] in optical imaging, focusing and guiding of light far below the diffraction limit,[5−7] in solar energy harvesting,[8−10] and in photocatalysis.[11]

Despite the vast promise of plasmonics, there are some unresolved challenges in this field. For instance, among the materials that show sharp resonances [narrow bandwidth (BW)], very few are suitable for sensing applications. In fact, Au has been the only practically useful metal because all other known plasmonic materials either have a tendency to degrade quickly (*e.g.*, Ag and Cu) or are extremely reactive (*e.g.*, Na, K) under ambient conditions. The remainder of metals, including the ferromagnetic elements, have nonexistent or highly damped visible plasmons.[12−14] Another challenge is how to control the various characteristics of a plasmon, such as its wavelength, scattering intensity, and BW. Last, but not least, is the ability to engineer good plasmonic properties in poor/nonplasmonic materials, as detailed in ref.[13] One particular case pertains to ferromagnetic systems, where there is a great desire to achieve dynamic control of localized surface plasmon resonance (LSPR) wavelength and BW by applying external magnetic fields. The absence of natural materials with both useful magnetic and optical properties has limited potential applications in imaging, computer memory, and metamaterials.[15−17] Until now, there is no direct

* Address correspondence to gduscher@utk.edu, ramki@utk.edu.

Received for review June 11, 2014 and accepted July 28, 2014.

Published online July 28, 2014
10.1021/nn5031719

evidence that plasmons with large scattering intensity in the visible or any other wavelength is possible in a ferromagnet. One way to achieve this goal is to design complex plasmonic materials, such as bi- or multimetallic nanostructures in which the optical properties come from the interaction between the various plasmon modes of the different components. For example, when two nanostructures of the same metal come in close proximity, their plasmons interact with each other leading to new hybridized plasmon modes.[18] More interesting behaviors are expected in interacting systems when the symmetry is broken by changing the size, shape, and type of materials involved in one or both of the nanostructures. One example is plasmon induced transparency,[19−22] analogous to the Fano resonance in atomic systems.[23] Fano resonance can be achieved by the interference of hybridized subradiant and super-radiant modes of asymmetric nanoparticle systems,[24] as well as interference of dark and bright modes.[24,25] The Fano effect has been observed in a wide variety of asymmetric structures involving strong plasmonic materials in multishell nanostructures[26,27] and cavities.[28] It has also been observed in contacting or noncontacting heterodimers of plasmonic noble metals.[29−36] However, heterodimers involving nonplasmonic materials have remained virtually unexplored.

Here, we report the observation of strong LSPRs in a nonplasmonic nanoparticle (NP), when in contact with another plasmonic material in the form of horizontally stacked nanoparticles on a substrate. We are not aware of any previous study that used such geometries to excite plasmons in a nonplasmonic material. Specifically, this was observed in pure Co or CoFe alloy (8 atom % Fe) NPs when they were in contact with Ag NPs. In contrast to the highly damped LSPR modes in the ultraviolet spectrum for Co and CoFe NPs, the LSPR in the bimetallic NPs is in the visible range with small BWs that are comparable to that in one of the best plasmonic materials, Ag.[13] We called this plasmon in a metal-ferromagnet nanoparticle as ferroplasmon (FP) for two reasons. First, this is a direct evidence for strong visible wavelength plasmons in a ferromagnet. Second, this phenomenon appears to be different from magnetoplasmonic effects in ferromagnets that arise from Kerr rotation.[16] As demonstrated later, the observation of LSPR in two different bimetals (Co−Ag and CoFe−Ag) of different diameters synthesized on two different substrates (conducting carbon and nonconducting Si_3N_4) suggests that the effects are free from experimental artifacts and represent a true property of the nanostructures. This study clearly demonstrates that bimetallic nanostructures are powerful ways to explore and discover new plasmonic materials.

The present results should not be confused with previous studies of alloys or heterodimers of nobel metals.[12−14] In the former case, the plasmon frequency basically interpolates between those of the constituent metals, damped by additional scattering from site-disorder (substitutional). In the latter case, sharp plasmons exist in both NPs; however, new plasmon modes develop in the hereodimers due to hybridization. In stark contrast, this study shows that sharp plasmon modes can be excited in materials with nonexistent/highly damped plasmon modes, when such a NP is in contact with another NP of a different material with sharp plasmons.

The choice of this particular bimetallic system was motivated by the long-term environmental stability of Co−Ag compared to pure Ag nanoparticles[37] and the immiscibility of the ferromagnetic elements (Co, Fe) with Ag, even at the nanoscale.[37−39] Electron energy-loss spectroscopy (EELS) in a scanning transmission electron microscope (STEM), which is a powerful tool to probe the local plasmonic behavior of nanostructures,[40,41] was used in this investigation. A monochromated electron source in the STEM made this technique even more useful for quantitative analysis of the data. Far-field optical spectra from the bimetal also showed evidence for strong LSPRs. A theoretical analysis using current plasmonic interaction models between spherical nanoparticles suggests that a Fano resonance could explain the ferroplasmon energy level. There is also the possibility that a dipole−dipole or hybridization interaction model could be sufficient, provided the particle shape is taken into consideration.

RESULTS

Experimental Observation of Ferroplasmons. In this study, we report results for pure Co as well as CoFe alloy (8 atom % Fe) NPs in contact with Ag NPs, as described in the Experimental Section. Typical experimental EELS spectra corresponding to marked locations on various nanoparticles (NPs) under consideration (CoFe−Ag, Ag, and CoFe on carbon substrates) are shown in Figure 1. Specifically, Figure 1(b−d) show high-angle annular dark field (HAADF) or Z-contrast images from the STEM of 98 nm CoFe−Ag, 64 nm Ag, and 30 nm CoFe NPs, respectively. The general structure of the CoFe−Ag NP shown in Figure 1b can be described as bimetallic with horizontal stacking of the two primary metals on the substrate plane. Completely phase segregated Ag and CoFe occupy distinctly separate regions, with the brighter region corresponding to Ag and the darker region to CoFe, as confirmed by the EELS composition maps (see the Supporting Information). The image contrast arises from the difference in their atomic numbers (*Z*), *i.e.*, *Z*-contrast. No evidence for miscibility (of either Co or Fe in Ag or *vice versa*) in the segregated nanoparticles was detected within the experimental resolution of 0.4 atom %. Similar elemental map studies have been reported earlier,[37,38] where it was shown

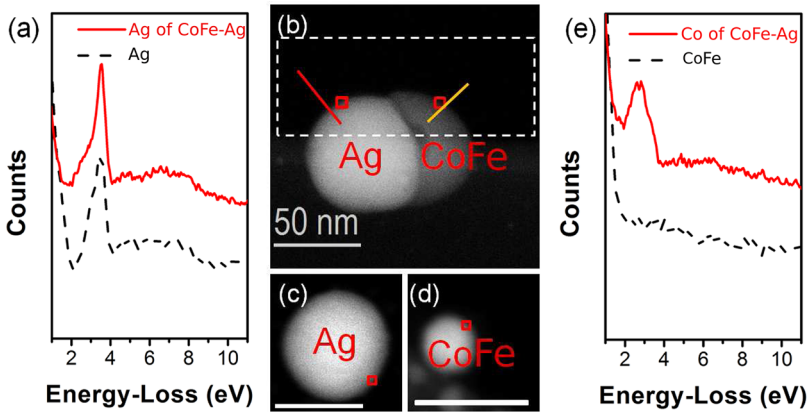

Figure 1. (a) Experimental EELS spectra from the surface of the Ag region in a CoFe−Ag NP (solid line) and isolated Ag NP (dashed line). HAADF image of (b) a CoFe−Ag bimetallic NP, (c) an isolated Ag NP, and (d) an isolated CoFe NP. (e) Experimental EELS spectra from the surface of the CoFe region in a CoFe−Ag NP (solid line) and isolated CoFe NP (dashed line). The spectra were taken from the regions marked by square-boxes in the respective NPs. The scale bar for each HAADF image is 50 nm. The dashed box shown in (b) represents the area from which the plasmon intensity maps, shown later in Figure 5, were constructed. All these NPS were on C substrates. The NPs shown in (b), (c), and (d) are of size 98 (along major axis), 64, and 30 nm, respectively.

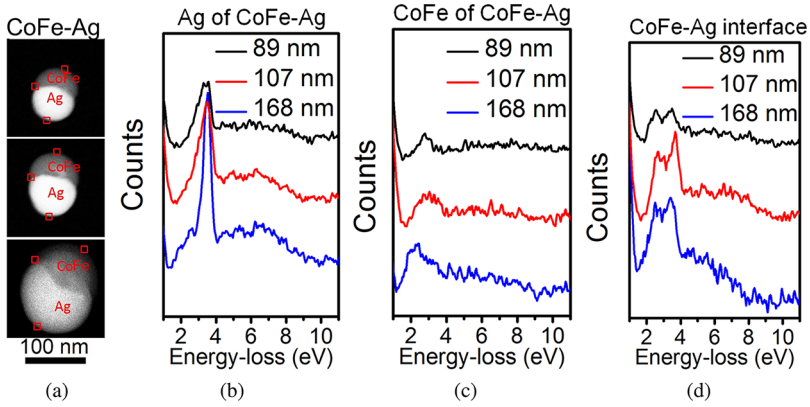

Figure 2. (a) HAADF image of various CoFe−Ag NPs on C-substrate, where the size of NP increases from top to bottom. The scale bar of 100 nm is the same for all images. EELS spectra from (b) the Ag side, (c) CoFe side, and (d) the interface between the CoFe and Ag of the CoFe−Ag NPs, as a function of particle diameter.

that Ag and Co occupy physically segregated regions in a NP due to (i) immiscibility and (ii) the nonequilibrium nature of the nanosecond laser dewetting technique. After elemental identification in the NP by core-loss EELS studies, low-loss EELS spectra in the imaging mode were acquired to obtain plasmon information.

In Figure 1a, EELS spectra taken from the square area marked by a box in Figure 1b from the Ag region of a CoFe−Ag (solid line), and isolated Ag NP (dashed line) are shown. Both spectra exhibit peaks in the visible range corresponding to the well-known surface plasmon in Ag. In contrast, the EELS spectrum from the CoFe side of a CoFe−Ag NP is entirely different from that taken from an isolated CoFe NP [Figure 1d], as shown in Figure 1e. In place of a featureless spectrum for the isolated CoFe NP, a strong and distinct peak at about 2.7 eV was observed in the CoFe region of the CoFe−Ag NP (Figure 1e, solid line). Henceforth, the 2.7 eV excitation in CoFe NPs in contact with Ag NPs will be referred to as ferroplasmon (FP) for reasons outlined in the introduction section.

To confirm that the strong FP peaks from the CoFe region of CoFe−Ag are a general feature of these NPs, 20 CoFe−Ag particles of different diameters were selected from random locations on the carbon substrate for the EELS studies. In Figure 2a, the HAADF images of three different diameter (89, 107, and 168 nm) CoFe−Ag particles on C-substrate are shown and the corresponding spectra from the (i) Ag surface, (ii) Co surface, and (iii) the interface between Ag and Co are shown in Figure 2b−d, respectively. The spectra correspond to the boxed regions marked in Figure 2a. All these particles show strong FP peaks in addition to the expected Ag peak. However, the FP peak positions varied slightly for the different diameter particles [Figure 3c]. Spectra from isolated Ag (31, 64, and 180 nm) and Co (10, 28, and 63 nm) NPs of different diameters also looked similar to those of Figure 1a,e (dashed lines), respectively. The detailed results are available in the Supporting Information.

To demonstrate that the appearance of the FP peak was not due to the small amount of Fe in the alloy or

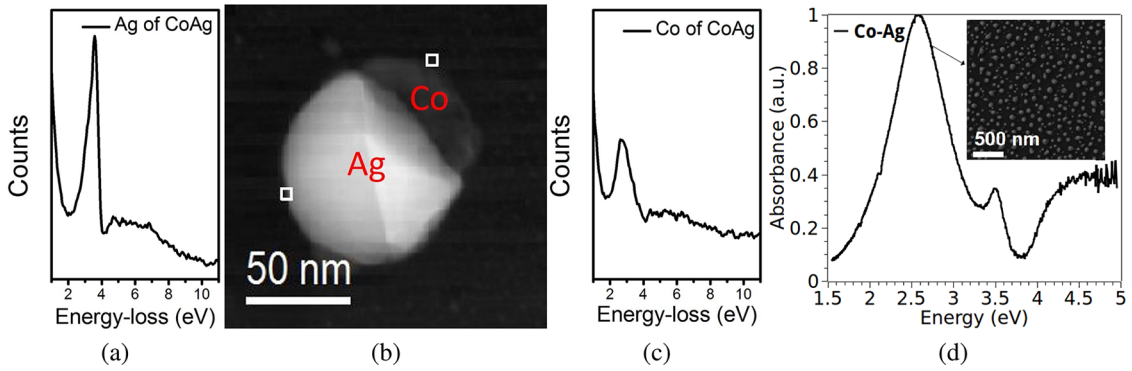

Figure 3. (a) Experimental EELS spectra from the marked location on the surface of the Ag region of the Co−Ag NP shown in (b). (b) HAADF image of an isolated Co−Ag NP on C-substrate. The marked regions correspond to the locations of the EELS spectra shown in (a) or (c). (c) Experimental EELS spectra from the marked location on the surface of the Co region of the Co−Ag NP shown in (b). (d) Far-field optical spectra for an ensemble of Co−Ag NPs on C substrate. An SEM image of the Co−Ag NP array is shown in the inset.

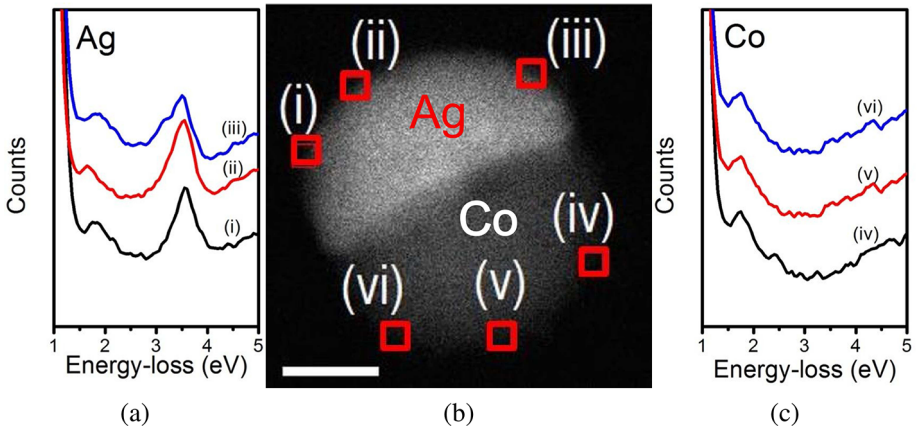

Figure 4. (a) Experimental EELS spectra from the various marked locations (numbered (i) to (iii)) on the surface of the Ag region of the Co−Ag NP on Si_3N_4 substrate shown in (b). (b) HAADF image of an isolated Co−Ag NP on Si_3N_4. The marked regions correspond to the locations of the EELS spectra shown in (a) or (c). The scale bar is 100 nm. (c) Experimental EELS spectra from various marked locations (numbered (iv) to (vi)) on the surface of the Co region of the Co−Ag NP shown in (b).

due to the conducting C-substrate, we prepared additional materials. One was Co−Ag NPs (*i.e.*, containing pure Co) on C-substrate, and another was Co−Ag NPs on an insulating Si_3N_4 substrate. In Figure 3b, the HAADF image of Co−Ag bimetal nanoparticle on C-substrate is shown, while the EELS spectrum from the Ag portion and the Co portion (marked by square boxes) are shown in Figure 3, panels a and c, respectively. Again the striking feature is that the EELS spectrum from the Co side of Co−Ag NP shows a strong and distinct peak at about 2.7 eV (Figure 3c), similar to the case for the CoFe−Ag NP presented in Figures 1 and 2. In Figure 3d, we also show the far-field optical absorption spectra of the array of Co−Ag NPs. The spectra was collected with normal incidence light over an area of 500 μm^2 and, therefore, represented an ensemble averaged information from the NP array. The array had a wide but monomodal size distribution, as depicted by the SEM image shown in the inset, with an average NP size of 105 ± 30 nm. This confirmed that a strong LSPR signal at 2.57 eV was also evident in the far field. Not too much significance should be attached to this small difference in energy (2.57 compared to 2.7 eV) between the optical and EELS data, since the former is an ensemble averaged energy from particles of different diameters and the latter from individual NPs of fixed diameters.

In Figure 4b, the HAADF image of a Co−Ag bimetal nanoparticle on Si_3N_4 substrate is shown. The EELS spectrum from the various marked locations of the Ag region (numbered i to iii on Figure 4b) are shown in Figure 4a, while that for the Co portion (numbered iv to vi on Figure 4b) are shown in Figure 4c. The spectrum from the Co region of the Co−Ag NPs was generally similar to those shown in Figure 2c, for the C-substrate, except for a red-shift to 1.8 eV for the Si_3N_4 substrate. This can be explained by the large difference in the dielectric permittivity of Si_3N_4 (4) compared to that of C (2.3) in the visible wavelength (see calculations provided in the Supporting Information). The background intensities in the EELS spectra for the Si_3N_4 substrate were comparatively higher than for the C-substrates since thick (60 nm) commercial Si_3N_4 substrates were used, in contrast to our lab-prepared thin (20 nm) C-substrates.

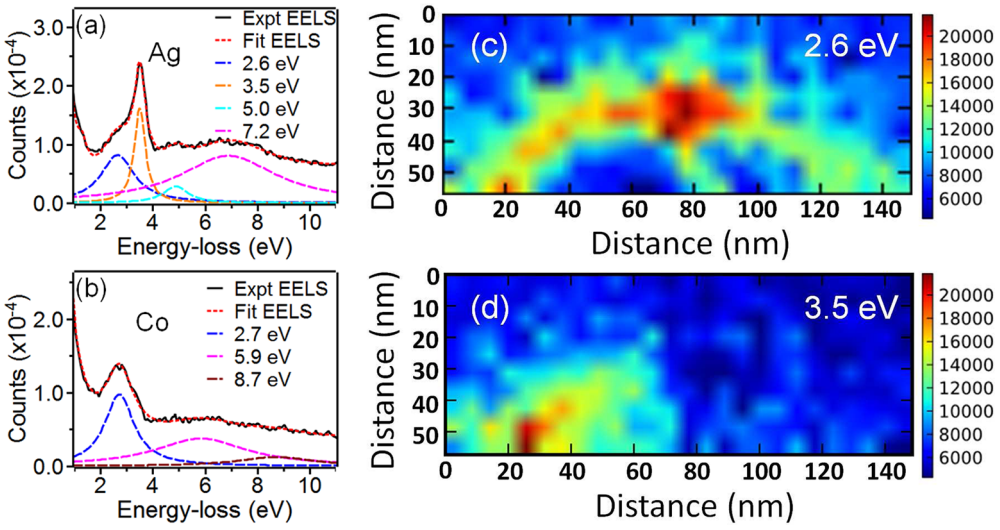

Figure 5. Experiment and fits to the EELS spectra from the surface of the CoFe−Ag nanoparticle taken at the positions marked by the square boxes in Figure 1b. (a) From the Ag region in a CoFe−Ag NP. The peak at 2.6 eV is similar to the FP, while another plasmon peak exists at 3.5 eV. (b) From the CoFe region in a CoFe−Ag NP. The large peak at 2.7 eV corresponds to the visible energy FP. (c and d) Spatial maps of the scattering intensities for the 2.6 ± 0.3 and 3.5 ± 0.4 eV plasmon modes over the CoFe−Ag NP region marked by a white rectangular box in Figure 1b. The *y*-axis is in nanometer and the right side of the figure shows the intensity scale (arbitrary units) used to map the surface plasmons.

On the basis of these experimental results, some important findings can be summarized. The first is that the EELS spectra from CoFe in CoFe−Ag (or from Co in Co−Ag) NPs are distinctly different from those for isolated CoFe (or Co) NPs; new, sharp LSPR in the visible range appears in the metal-ferromagnet bimetals compared to a featureless spectrum for isolated CoFe (or Co) NPs. Compared to CoFe (or Co), the behavior of Ag in the bimetal is not significantly different (except for slight shifts in the peak position) from isolated Ag NPs. The far-field optical data also showed strong LSPR peaks in the visible energy range for the Co−Ag bimetal. These new features in the bimetals measured by the EELS and optical techniques appear to be an intrinsic property of the nanostructures, independent of measurement artifacts, substrate type, and small alloying effects (Co with Fe).

Characteristics of the Plasmon Peaks. The EELS spectra from the CoFe and Ag regions were analyzed further by fitting several Lorentzian peaks (see the Supporting Information for details), as shown in Figure 5a,b. In each case, the experimentally acquired spectra are shown by the solid curves, fitted spectra by dotted curves, and Lorentzian peak fits corresponding to the individual plasmon modes by dashed curves. The fits should be judged in the context of the energy resolution (0.15 eV) of the EELS measurements (see Experimental Section). The EELS spectra from the Ag region in CoFe−Ag (Figure 5a]) show peaks at 2.6 eV (BW of 1.3 eV), 3.5 eV (BW of 0.6 eV), and 5.0 eV (BW of 1.0 eV). On the other hand, spectra from the CoFe region in CoFe−Ag (Figure 5b) show a strong, sharp plasmon peak at 2.7 eV (BW of 1.6 eV) and a weak, broad peak at 5.9 eV (BW of 4.6 eV). In contrast, the EELS spectra of the isolated CoFe NP (Figure 1e), were best fitted by a very weak and extremely broad plasmon peak at 3.8 eV (BW of 6.5 eV), as shown in the Supporting Information Figure 6c. Likewise, the EELS spectra from the isolated Ag NP shown in Figure 1a could be fitted by peaks at 3.0 (BW of 0.7 eV) and 3.5 eV (BW of 0.5 eV) [Supporting Information Figure 6a].

Next, we quantified the scattering intensities of the various plasmon peaks observed in Figure 5a,b in the range of ~2 to 4 eV. To directly compare the scattering intensities, the scanning parameters for every case were kept identical, such as a pixel area (5.7×5.7 nm^2), electron beam current (7 pA), and total exposure time (0.1 s) for each pixel. Panels c and d of Figure 5 are the scattering intensity maps for energies of 2.6 ± 0.3 and 3.5 ± 0.4 eV, respectively, acquired from the boxed region (white dashed lines) shown in Figure 1b. The energy deviation represented the natural spread in the peak positions for the cases shown in Figure 1a,e. As evident in Figure 5c, the scattering intensity for the 2.6 eV excitation is highest at the particle/vacuum interface, compared to the interior of the NP. Another important feature is that *the overall scattering intensity of the 2.6 eV plasmon in the CoFe region is similar to that in the Ag region* (Figure 5c).

Figure 5d shows the spatial intensity map for the 3.5 eV plasmon, which is high on the surface of the Ag region, but not present in the CoFe region. It is consistent with the characteristic of isolated Ag NPs at the same energy. This plasmon mode is due to quadrupole interactions in Ag,[42,43] and was also evident in the optical far-field spectra of Figure 3d.

Surface Plasmon Energy Diagram. To differentiate the surface plasmons from the bulk plasmons, we quantified

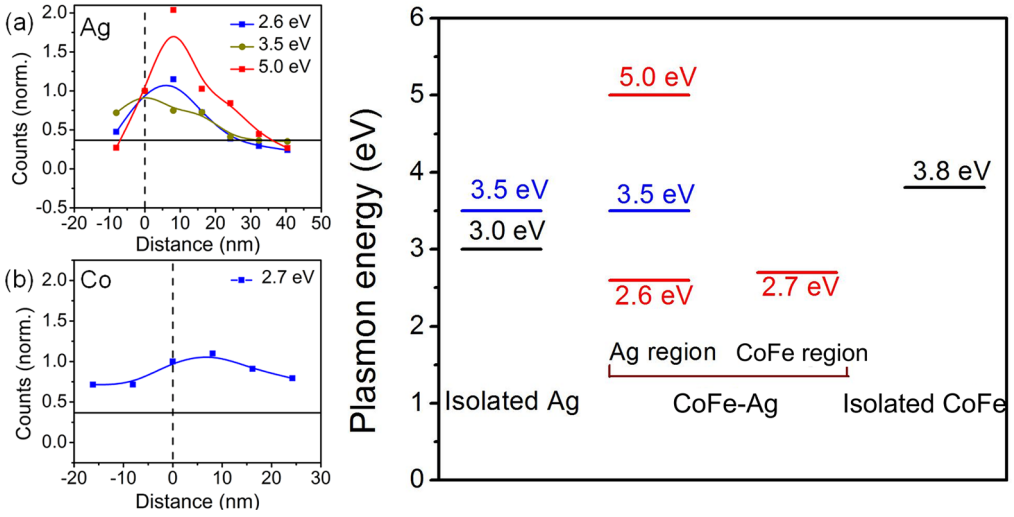

Figure 6. (a and b) Spatial dependence of the normalized intensities (w.r.t. the intensity at the surface) of various energy loss peaks within and outside of a CoFe−Ag NP (the vertical dashed line is the particle/vacuum interface and the horizontal solid line defines where the intensity has dropped to 1/e). (a) Surface and bulk plasmon decay trend from the Ag surface/vacuum interface and (b) surface and bulk plasmon decay trend from the Co surface/vacuum interface. The decay intensity measurements were made in the same was as those shown in Figure 1b, going from bulk of CoFe−Ag NP to vacuum. (c) Surface plasmon energy diagram showing the measured energy levels in Ag and CoFe regions of bimetallic CoFe−Ag, isolated Ag, and isolated CoFe NPs.

the intensity as a function of distance from the particle interface. It is known that bulk plasmon excitations are confined inside the material and do not extend significantly outside the surface.[44] On the other hand, surface plasmons show a delocalization of electronic charge density that decays slowly into the vacuum, usually extending far beyond the material surface. It is generally acknowledged that surface plasmon intensities should be $\geq 1/e$ at a distance of $0.2D$ from the surface, where D is the particle diameter.[45] Additionally, the intensities of the surface plasmons should decrease inside the particle, and increase for the bulk plasmons. The results of our measurements are shown in Figure 6a for the Ag-side and in Figure 6b for the CoFe side of the NP, with the spectra taken along the solid lines shown in the HAADF image (Figure 1b). The spatial intensity distributions indicate that a few specific excitations (such as at 2.6, 3.5, and 5.0 eV in the Ag region and 2.7 eV in the CoFe region) retain large intensities even at a distance of 0.2D away from the particle-vacuum interface, and they decay upon entering the particle interior. The other excitations decrease by many orders of magnitude within a distance of only ~10 nm from the particle surface. It should be emphasized that our measurement of the decay length is based on the near-field interaction of the electron beam with the plasmons and, therefore, could result in different values of the decay length when compared to measurements made using far-field spectroscopy.[44−46]

Based on the above analysis, we constructed a surface plasmon energy diagram for the CoFe−Ag, CoFe, and Ag particles, respectively, as shown in Figure 6c. (Since no substantial difference was observed between pure Co and CoFe (8 atom %) alloy NPs, the diagram is similar for the Co−Ag case.) *It is evident that the excited plasmons in the Ag and CoFe regions of the CoFe−Ag NP are distinctly different from those in isolated Ag and CoFe NPs*. The surface plasmon at 3.5 eV in the isolated *Ag* NP remains unchanged in the *Ag* region of CoFe−Ag. This plasmon excitation was not supported in CoFe at all, as was shown earlier in Figure 5d. Instead, a strong excitation at 2.7 eV, with characteristics of LSPR, appeared in the CoFe region of the composite NPs. Accordingly, the plasmons excited at 3.0 and 3.5 eV in isolated Ag NPs; 2.6, 3.5, and 5.0 eV in the Ag region of the CoFe−Ag NPs; 3.8 eV in isolated CoFe NPs; and 2.7 eV in the CoFe region of CoFe−Ag NPs were identified as localized surface plasmons.

DISCUSSION

To understand the possible reasons underlying this completely unexpected discovery, we focused primarily on the ability of existing models of plasmonic interactions toward predicting the 2.7 eV ferroplasmon observed in the Co−Ag (and CoFe−Ag) NPs. Plasmonic interaction could arise due to coupling between the same polarization modes (dipole−dipole, quadrupole−quadrupole, *etc.*) or among different modes (dipole−quadrupole, *etc.*). A simple way to understand the physics of the coupling is to consider two interacting Hertzian dipoles, as has been used successfully to describe the electromagnetic energy transfer between nanoparticles.[47] One of the limitations of this dipole−dipole interaction (DDI) model is that it only takes into account the near-field dipole interaction or Förster field, but neglects the interaction of other modes of oscillation of the system. Alternatively, a model based on plasmon hybridization (PH) between two spherical

particles could also be used,[18] which is analogous to the interaction between aggregates of organic molecules that leads to a shift in energy levels. In the hybridization model, the coupling can be viewed as an instantaneous Coulomb interaction between the surface charge densities of the various components. For a solid metal sphere, the charge density can be expressed as $\sigma(\Omega,t) = n_o\, e \sum_{lm}(1/R_i^3)^{1/2} S_{lm}(t) Y_{lm}(\Omega)$, [48] where R_i is the radius of the particle i, $Y_{lm}(\Omega)$ is the spherical harmonic of the solid angle, Ω, $S_{lm}(t)$ is the deformation, and n_o is the electron density. The charge distribution will have the symmetry of the specific angular momentum l and azimuthal quantum number m. The values of m and l determine the character of the surface charge distribution; for example, for the dipole mode of oscillation $l = 1$, and so on. With this approach, the interaction is diagonal in the azimuthal quantum number, which means that the plasmons with different m decouple, and the interaction reduces to the coupling of the different l. The problem, therefore, reduces to an eigenvalue problem. In the model, we used the condition for surface plasmons within the Drude limit, where the free electron response of the metals can be approximated by $\varepsilon = \{\varepsilon_\infty + [\omega_p^2/(\omega^2 + i\gamma\omega)]\}$. In this equation, the interband transition is taken into account by adding a high frequency part given by ε_∞, with ω_p corresponding to the bulk plasma frequency of the metal and γ to the electron relaxation time. With this, the energies of the surface plasmons of the isolated metal NPs can be approximated by $\omega_S = \omega_p\{l/[(l+1)\varepsilon_h + l\varepsilon_\infty]\}^{1/2}$. In this equation, ε_h represents the dielectric permittivity of the host, and we used a value of 2.75 for an effective surrounding dielectric of the Carbon and vacuum system.[49] The values for the interband contributions were taken as 1.0 and 3.8 for Co and Ag, respectively,[50,51] while the bulk plasmon frequencies for Ag and Co were taken as 9.165 and 9.74 eV.[13,50] This translated into LSPR modes at 3.0 and 3.8 eV for Ag and Co, respectively, consistent with our EELS measurements. We obtained the following pairs of energy levels (Supporting Information Figure 13a): For the longitudinal case ($l = 2$), the symmetric bright mode σ has $E = 2.5$ eV and the antisymmetric dark mode σ^* has $E = 4.2$ eV, while for the transverse case ($l = 1$), antisymmetric dark mode π^* has $E = 3.94$ eV and the symmetric bright mode π has $E = 2.84$ eV. Therefore, an important conclusion could be drawn for the PH model. The predicted bright mode at energy 2.84 eV appears to be the closest to our experimentally observed value of 2.7 eV. Interestingly, we found that the DDI interaction gave identical results to the PH (see Supporting Information Figure 13b). While one can argue that there is a reasonably good agreement in predicting the FP energy, it appears that these approaches (PD and DDI) are not completely satisfactory since the EELS experiments do not reveal the other predicted dark modes (4.2 and 3.94 eV) or the other bright mode (2.5 eV).

Another interaction approach is that of Fano interference (FI), in which interference between various hybridized modes can lead to a new resonance. For this to happen, there must be spectral and spatial overlap between bright and dark modes in the bimetal NP.[24] From our PH model results, we note that the σ modes cannot interfere with the π modes because they are orthogonal to each other, and interferences can occur only within the individual modes. Therefore, in our model, two possible interactions exist. One is the interference between the dark mode corresponding to the π^*-type excitation with 3.9 eV, and the π bright mode excitation with 2.8 eV. The other is interference between the dark σ^* with 4.1 eV and the bright σ mode with energy 2.5 eV. Using the methods outlined in ref 24 and detailed in the Supporting Information, the results for the $\pi-\pi^*$ case can be estimated by using the coupling strength (c) and the intrinsic damping term γ_d, as free parameters. A value of the Fano resonance corresponding to an energy similar to the measured experimental energy of 2.7 eV can indeed be obtained. However, given that there are two free parameters in this calculation, one could question the quantitative accuracy of our analysis. Analysis of the $\sigma-\sigma^*$ case (see the Supporting Information for details) shows that a 5 eV peak may be obtained in the EELS, which, in our experiments, were observed only on the Ag side of the bimetal NP. Clearly, like our previous analysis using the PH (or DDI) models, the Fano-interference may be a possibility, but is also subject to some uncertainty at this stage.

We suggest two possible reasons why our experimental discovery may not be quantifiable by the above outlined theoretical methods. The first is that our model calculations relied on a spherical nanoparticle shape. Presently, there is no analytical approach to account for the complex shapes seen in our experiment. Therefore, we have performed a calculation by assuming that a numerical factor α can be introduced into the PH interaction integral or the DDI Forster field to take into consideration deviations from sphericity. The result of this calculation (presented in the Supporting Information) shows that, by using an $\alpha = 2$ for the DDI or $\alpha = 1.5$ for the PH interaction models, one can generate a plasmon at 2.7 eV, identical to the EELS experimental value. A second aspect of our analysis is the use of a noncontacting geometry, *i.e.*, the implicit assumption that the contact between Ag and Co does not influence the interaction process. It is quite possible that the contact potential between the metals could play a role in the final analysis (and for example determine the coupling parameter c used in the Fano calculations). Spilling of electrons from one metal to the other or quantum mechanical tunneling at the interface may influence the plasmon interaction between the two metals.[52] As stated at the start of this discussion, we were focused on identifying whether

the ferroplasmon arises due to an interaction between the particles. While this appears to be partly successful from our analysis, future studies on bimetal systems that are aimed at investigating the role of shape and materials will likely shed more light on which of the various mechanisms, *i.e.*, the Fano interference, hybridization, or dipole−dipole interaction, is the more likely case. Therefore, it must be concluded that new theoretical ideas are needed for a quantitative explanation of this experimental discovery.

CONCLUSION

In conclusion, this study experimentally demonstrates ferroplasmons, which we define as intense localized surface plasmon resonances in metal-ferromagnetic nanoparticles [such as the NPs of Ag in contact with NPs of Co or CoFe alloy (8 atom % Fe)]. The ferroplasmons have energies in the visible range, with large scattering intensities and extremely narrow bandwidths, that are absent in isolated Co or CoFe alloy NPs. The bimetal nanoparticles also show a strong visible energy plasmon in the far-field optical spectra. A qualitative assessment of the origin of the ferroplasmon was made based on existing models of plasmon interactions, but a full quantitative description will likely require new theoretical ideas to account for the shape and physical contact of the nanoparticles. Overall, these results demonstrate that exploration of plasmonic and nonplasmonic metal NPs in contact can lead to new and unexpected optical properties, distinctly different from their constituent metals. Therefore, this work opens a previously under explored avenue, which is to combine plasmonic and nonplasmonic systems, to widen the choice of photonic materials for new as well as existing applications.

EXPERIMENTAL SECTION

Nearly hemispherical bimetallic CoFe (8 atom % Fe)−Ag or Co−Ag NPs on an electron transparent carbon substrate (20 nm thickness) were prepared by a synthesis method that combines pulsed laser dewetting with a carbon float-off technique (details in the Supporting Information). The control samples of isolated Ag, CoFe, and Co NPs were also made by the same synthesis method. We also prepared Co−Ag NPs on insulating Si_3N_4 substrates, as presented in Figure 4. The Si_3N_4 TEM grid substrates were commercially obtained from Ted Pella and the thickness was measured in the TEM to be 60 nm. We also verified that the plasmonic properties of Co and CoFe were similar (see the Supporting Information). The plasmonic characteristics of the bimetallic NPs were investigated as a function of position across their cross sections by electron energy-loss spectroscopy (EELS) in a scanning transmission electron microscope (STEM). The spatial resolution for these measurements was about 1 nm. The particles selected in this study were at the substrate edge to reduce the contribution of the substrate. No evidence for any substrate material-related phase was observed following the laser synthesis. To rule out any conducting substrate related artifacts, studies were also made on NPs synthesized on an insulating electron transparent substrate of Si_3N_4; similar results were obtained. The STEM (Zeiss Libra200) was equipped with a monochromator that provided an extremely high energy resolution (150 meV) and reduced zero-loss peak (ZLP) tails, which, in turn, gave superb low-loss spectra with excellent signal-to-noise ratio. The state-of-the-art quality of the low-loss spectrum allowed to profile the ZLP with a well-defined analytical function and to separate it out from the remainder of the spectrum to obtain high-resolution plasmon spectra (details in Supporting Information). The low-loss spectra were analyzed by fitting Lorentzian functions corresponding to each plasmon peak, which, in turn, provided the quantitative measure of the plasmon energy, BW, and scattering intensity from every position within a single nanoparticle. The far-field optical spectra was obtained with normal incidence unpolarized broadband light *via* a fiber coupled ocean optics HR2000+ES spectrometer.

Conflict of Interest: The authors declare no competing financial interest.

Acknowledgment. For the experimental work performed on various substrates as well as the analysis of the work, we acknowledge discussions with Dr. Rich Hammond and support by the Army Research Office through grant W911NF-13-1-0428. For the characterization and analysis portion of this work, the authors thank the Joint Institute of Advanced Materials (JIAM) at University of Tennessee-Knoxville (UTK) and Grant CNMS2013-284 at the Center for Nanophase Materials Science, which is sponsored at ORNL by the Scientific User Facilities Division, Office of Basic Energy Sciences, U.S. Department of Energy. For the materials synthesis aspects of this work, the authors also acknowledge support by the Sustainable Energy Education and Research Center, TN-SCORE, Center for Materials Processing, and the NSF through Grant CMMI-0855949. S.Y. was supported by NSF EAGER Grant CBET-1349507. G.D. acknowledges support by the U.S. Department of Energy, Basic Energy Sciences, Materials Sciences and Engineering Division under Award No. ERKCS81.

Supporting Information Available: The details of experimental procedures, magnetic measurements of NPs, core-loss EELS for elemental mapping, low-loss EELS quantification procedure, plasmon decay plots, Ag and Co NP size-dependence of surface plasmons, electron beam damage effects on NPs, theoretical plasmon interaction analysis by (i) plasmon hybridization and (ii) dipole−dipole interaction model. This material is available free of charge *via* the Internet at http://pubs.acs.org.

REFERENCES AND NOTES

1. Zhang, X.; Shah, N.; Van Duyne, R. Sensitive and Selective Chem/Bio Sensing Based on Surface-Enhanced Raman Spectroscopy (SERS). *Vib. Spectrosc.* **2006**, *42*, 2–8.
2. Primera-Pedrozo, O.; Jerez-Rozo, J. I.; Cruz-Montoya, E.; Luna-Pineda, T.; Pacheco-Londono, L. C.; Hernandez-Rivera, S. Nanotechnology-Based Detection of Explosives and Biological Agents Simulants. *IEEE Sens. J.* **2008**, *8*, 963–973.
3. Jackson, J. B.; Halas, N. J. Surface-Enhanced Raman Scattering on Tunable Plasmonic Nanoparticle Substrates. *Proc. Natl. Acad. Sci. U.S.A.* **2004**, *101*, 17930–17935.
4. Zhang, H.; Harpster, M. H.; Wilson, W. C.; Johnson, P. A. Surface-Enhanced Raman Scattering Detection of DNAs Derived from Virus Genomes using Au-Coated Paramagnetic Nanoparticles. *Langmuir* **2012**, *28*, 4030–4037.
5. Gramotnev, D. K.; Bozhevolnyi, S. I. Plasmonics Beyond the Diffraction Limit. *Nat. Photonics* **2010**, *4*, 83–91.
6. Lezec, H. J.; Thio, T. Diffracted Evanescent Wave Model for Enhanced and Suppressed Optical Transmission through Subwavelength Hole Arrays. *Opt. Express* **2004**, *12*, 3629–3651.
7. Specht, M.; Pedarnig, J. D.; Heckl, W. M.; Hansch, T. W. Scanning Plasmon Near-Field Microscope. *Phys. Rev. Lett.* **1992**, *68*, 476–479.
8. Pillai, S.; Catchpole, K. R.; Trupke, T.; Green, M. A. Surface Plasmon Enhanced Silicon Solar Cells. *J. Appl. Phys.* **2007**, *101*, No. 093105 (1−8).

9. Ferry, V. E.; Munday, J. N.; Atwater, H. A. Design Considerations for Plasmonic Photovoltaics. *Adv. Mater.* **2010**, *22*, 4794–4808.
10. Laux, E.; Genet, C.; Skauli, T.; Ebbesen, T. W. Plasmonic Photon Sorters for Spectral and Polarimetric Imaging. *Nat. Photonics* **2008**, *2*, 161–164.
11. Linic, S.; Christopher, P.; Ingram, D. Plasmonic-Metal Nanostructures for Efficient Conversion of Solar to Chemical Energy. *Nat. Mater.* **2011**, *10*, 911–921.
12. Blaber, M.; Arnold, M.; Ford, M. A Review of the Optical Properties of Alloys and Intermetallics for Plasmonics. *J. Phys: Condens. Matter* **2010**, *22*, No. 143201 (1−15).
13. West, P. R.; Ishii, S.; Naik, G. V.; Emani, N. K.; Shalaev, V. M.; Boltasseva, A. Searching for Better Plasmonic Materials. *Laser Photonics Rev.* **2010**, *4*, 795–808.
14. Cortie, M. B.; McDonagh, A. M. Synthesis and Optical Properties of Hybrid and Alloy Plasmonic Nanoparticles. *Chem. Rev.* **2011**, *111*, 3713–3735.
15. Alu, A.; Engheta, N. The Quest for Magnetic Plasmons at Optical Frequencies. *Opt. Express* **2009**, *17*, 5723–5730.
16. Temnov, V. V.; Armelles, G.; Woggon, U.; Guzatov, D.; Cebollada, A.; Garcia-Martin, A.; Garcia-Martin, J.-M.; Thomay, T.; Leitenstorfer, A.; Bratschitsch, R. Active Magneto-Plasmonics in Hybrid Metal-Ferromagnet Structures. *Nat. Photonics* **2010**, *4*, 107–111.
17. Lukyanchuk, B.; Zheludev, N. I.; Maier, S. A.; Halas, N. J.; Nordlander, P.; Giessen, H.; Chong, C. T. The Fano Resonance in Plasmonic Nanostructures and Metamaterials. *Nat. Mater.* **2010**, *9*, 707–715.
18. Prodan, E.; Radloff, C.; Halas, N. J.; Nordlander, P. A Hybridization Model for the Plasmon Response of Complex Nanostructures. *Science* **2003**, *302*, 419–422.
19. Liu, N.; Langguth, L.; Weiss, T.; Kastel, J.; Fleischhauer, M.; Pfau, T.; Giessen, H. Plasmonic Analogue of Electromagnetically Induced Transparency at the Drude Damping Limit. *Nat. Mater.* **2009**, *8*, 758–762.
20. Litvak, A. G.; Tokman, M. D. Electromagnetically Induced Transparency in Ensembles of Classical Oscillators. *Phys. Rev. Lett.* **2002**, *88*, No. 095003 (1−4).
21. Zhang, S.; Genov, D. A.; Wang, Y.; Liu, M.; Zhang, X. Plasmon-Induced Transparency in Metamaterials. *Phys. Rev. Lett.* **2008**, *101*, No. 047401 (1−4).
22. Harris, S. E. Electromagnetically Induced Transparency. *Phys. Today* **1997**, *50*, 36–42.
23. Fano, U. Effects of Configuration Interaction on Intensities and Phase Shifts. *Phys. Rev.* **1961**, *124*, 1866–1878.
24. Gallinet, B.; Martin, O. J. F. Influence of Electromagnetic Interactions on the Line Shape of Plasmonic Fano Resonances. *ACS Nano* **2011**, *5*, 8999–9008.
25. Miroshnichenko, A. E.; Flach, S.; Kivshar, Y. S. Fano Resonances in Nanoscale Structures. *Rev. Mod. Phys.* **2010**, *82*, 2257–2298.
26. Mukherjee, S.; Sobhani, H.; Lassiter, J. B.; Bardhan, R.; Nordlander, P.; Halas, N. J. Fanoshells: Nanoparticles with Built-in Fano Resonances. *Nano Lett.* **2010**, *10*, 2694–2701.
27. Zhang, J.; Zayats, A. Multiple Fano Resonances in Single-Layer Nonconcentric Core-Shell Nanostructures. *Opt. Express* **2013**, *21*, 8426–8436.
28. Cetin, A. E.; Altug, H. Fano Resonant Ring/Disk Plasmonic Nanocavities on Conducting Substrates for Advanced Biosensing. *ACS Nano* **2012**, *6*, 9989–9995.
29. Bachelier, G.; Antoine, I. R.; Benichou, E.; Jonin, C.; Del Fatti, N.; Vallee, F.; Brevet, P. F. Fano Profiles Induced by Near-Field Coupling in Heterogeneous Dimers of Gold and Silver Nanoparticles. *Phys. Rev. Lett.* **2008**, *101*, No. 197401 (1−4).
30. Chen, F.; Alemu, N.; Johnston, R. L. Collective Plasmon Modes in a Compositionally Asymmetric Nanoparticle Dimer. *AIP Adv.* **2011**, *1*, No. 032134 (1−16).
31. Encina, E. R.; Coronado, E. A. On the Far Field Optical Properties of Ag-Au Nanosphere Pairs. *J. Phys. Chem. C* **2010**, *114*, 16278–16284.
32. Encina, E. R.; Coronado, E. A. Near Field Enhancement in Ag Au Nanospheres Heterodimers. *J. Phys. Chem. C* **2011**, *115*, 15908–15914.
33. Rodriguez, O. P.; Pal, U.; Quiles, M. C.; Fernandez, L. R.; Garriga, M.; Alonso, M. I. Enhanced Fano Resonance in Asymmetrical Au:Ag Heterodimers. *J. Phys. Chem. C* **2011**, *115*, 6410–6414.
34. Bigelow, N. W.; Vaschillo, A.; Camden, J. P.; Masiello, D. J. Signatures of Fano Interferences in the Electron Energy Loss Spectroscopy and Cathodoluminescence of Symmetry-Broken Nanorod Dimers. *ACS Nano* **2013**, *7*, 4511–4519.
35. Brown, L. V.; Sobhani, H.; Lassiter, J. B.; Nordlander, P.; Halas, N. J. Heterodimers: Plasmonic Properties of Mismatched Nanoparticle Pairs. *ACS Nano* **2010**, *4*, 819–832.
36. Mirin, N. A.; Bao, K.; Nordlander, P. Fano Resonances in Plasmonic Nanoparticle Aggregates. *J. Phys. Chem. A* **2009**, *113*, 4028–4034.
37. Sachan, R.; Ramos, V.; Malasi, A.; Yadavali, S.; Bartley, B.; Duscher, G.; Kalyanaraman, R. Oxidation Resistant Ag Nanoparticles for Ultrastable Plasmonic Applications. *Adv. Mater.* **2013**, *25*, 2045–2050.
38. Sachan, R.; Yadavali, S.; Shirato, N.; Krishna, H.; Ramos, V.; Duscher, G.; Pennycook, S. J.; Gangopadhyay, A. K.; Garcia, H.; Kalyanaraman, R. Self-Organized Bimetallic Ag-Co Nanoparticles With Tunable Localized Surface Plasmons Showing High Environmental Stability and Sensitivity. *Nanotechnology* **2012**, *23*, No. 275604 (1−8).
39. Krishna, H.; Shirato, N.; Yadavali, S.; Sachan, R.; Strader, J.; Kalyanaraman, R. Self-Organization of Nanoscale Multilayer Liquid Metal Films: Experiment and Theory. *ACS Nano* **2011**, *5*, 470–476.
40. Nelayah, J.; Kociak, M.; Stephan, O.; de Abajo, F. J. G.; Tence, M.; Henrard, l.; Taverna, D.; Santos, I. P.; Liz-Marzan, L. M.; Colliex, C. Mapping Surface Plasmons on a Single Metallic Nanoparticle. *Nat. Phys.* **2007**, *3*, 348–353.
41. Koh, A. L.; Bao, K.; Khan, I.; Smith, W. E.; Kothleitner, G.; Nordlander, P.; Maier, S. A.; McComb, D. W. Electron Energy-Loss Spectroscopy (EELS) of Surface Plasmons in Single Silver Nanoparticles and Dimers: Influence of Beam Damage and Mapping of Dark Modes. *ACS Nano* **2009**, *3*, 3015–3022.
42. Kreibig, U.; Vollmer, M. *Optical Properties of Metal Clusters*; Springer Series in Material Science: Germany, 1995.
43. Malasi, A.; Kalyanaraman, R.; Garcia, H. From Mie to Fresnel through Effective Medium Approximation with Multipole Contributions. *J. Opt.* **2014**, *16*, No. 065001 (1−9).
44. Zhou, W.; Pennycook, S. J.; Idrobo, J. C. Localization of Inelastic Electron Scattering in the Low-Loss Energy Regime. *Ultramicroscopy* **2012**, *119*, 51–56.
45. Jain, P. K.; El-Sayed, M. A. Plasmonic Coupling in Noble Metal Nanostructures. *Chem. Phys. Lett.* **2010**, *487*, 153–164.
46. Nicoletti, O.; Wubs, M.; Mortensen, N. A.; Sigle, W.; van Aken, P. A.; Midgley, P. A. Surface Plasmon Modes of a Single Silver Nanorod: an Electron Energy Loss Study. *Opt. Express* **2011**, *19*, 15371–15379.
47. Brongersma, M. L.; Hartman, J. W.; Atwater, H. A. Electromagnetic Energy Transfer and Switching in Nanoparticle Chain Arrays below the Diffraction Limit. *Phys. Rev. B* **2000**, *62*, R16356–R16359.
48. Nordlander, P.; Oubre, C.; Prodan, E.; Li, K.; Stockman, M. I. Plasmon Hybridization in Nanoparticle Dimers. *Nano Lett.* **2004**, *4*, 899–903.
49. Garcia, H.; Sachan, R.; Kalyanaraman, R. Optical Plasmon Properties of Co-Ag Nanocomposites Within The Mean-Field Approximation. *Plasmonics* **2012**, *7*, 137–141.
50. Clavero, C.; Cebollada, A.; Armelles, G.; Huttel, Y.; Arbiol, J.; Peiro, F.; Cornet, A. Size Effects in the Magneto-Optical Response of Co Nanoparticles. *Phys. Rev. B* **2005**, *72*, No. 024441 (1−6).
51. Gai, H.; Wang, J.; Tian, Q. Modified Debye Model Parameters of Metals Applicable for Broadband Calculations. *Appl. Opt.* **2007**, *46*, 2229–2233.
52. Esteban, R.; Borisov, A. G.; Nordlander, P.; Aizpurua, J. Bridging Quantum and Classical Plasmonics with a Quantum-Corrected Model. *Nat. Commun.* **2012**, *3* No. 825 (1−9).